Applied Catalysis B: Environmental 246 (2019) 277–283

Contents lists available at ScienceDirect

Applied Catalysis B: Environmental

journal homepage: www.elsevier.com/locate/apcatb

Cross-double dumbbell-like Pt–Ni nanostructures with enhanced catalytic performance toward the reactions of oxygen reduction and methanol oxidation

Wenhao Gong[a], Zheng Jiang[a], Rifeng Wu[a], Yang Liu[a], Lei Huang[a], Ning Hu[a], Panagiotis Tsiakaras[b,c,d,*], Pei Kang Shen[a,**]

[a] Collaborative Innovation Center of Sustainable Energy Materials, Guangxi Key Laboratory of Electrochemical Energy Materials, State Key Laboratory of Processing for Non-ferrous Metal and Featured Materials, Guangxi University, Nanning, 530004, PR China

[b] Laboratory of Materials and Devices for Electrochemical Power Industry, Ural Federal University, 19 Mira Str., Yekaterinburg, 620002, Russia

[c] Laboratory of Electrochemical Devices based on Solid Oxide Proton Electrolytes, Institute of High Temperature Electrochemistry (RAS), Yekaterinburg, 620990, Russia

[d] Laboratory of Alternative Energy Conversion Systems, Department of Mechanical Engineering, School of Engineering, University of Thessaly, Pedion Areos, 38834, Greece

ARTICLE INFO

Keywords:
Cross double dumbbell-like nanostructure
Bimetallic alloy
Oxygen reduction reaction
Methanol oxidation reaction

ABSTRACT

Investigating on well-defined structure-engineering and atomic arrangement of fuel cell catalysts with high activity has attracted considerable research interest the last decade. Specially, unique nanostructures, which possess high surface-to-volume ratio and high atomic utilization have been emerged as promising candidate catalysts.

Herein, we have successfully synthesized Pt–Ni cross double dumbbell-like nanostructures (Pt-Ni CDDNs) via a facile one-pot synthesis route and a kinetic control with surface capping. It is found that the as-prepared Pt–Ni alloy nanostructures exhibit an enhanced catalytic activity toward oxygen reduction reaction (ORR) and methanol oxidation reaction (MOR) in comparison with commercial Pt/C catalysts. The excellent electrooxidation property is attributed to the synergistic effect between Pt and Ni atoms, as well as high specific surface area of dumbbell-like nanostructures with multiple nanosheets. The present work provides new opportunities for the rational design of bimetallic nanomaterials with enhanced catalytic performance.

1. Introduction

Polymer electrolyte membrane fuel cells (PEMFCs) exhibit great potential as a renewable energy conversion devices for powering portable electronic appliances and vehicles. Due to their high energy conversion efficiency and zero greenhouse gas emissions, developing high-efficiency electrocatalysts for the cathodic oxygen reduction reaction (ORR) and for the anodic methanol oxidation reaction (MOR) is a vital step for the application of fuel cells [1–9]. Recently, noble metal platinum (Pt) nanomaterials are the widespread catalysts because of their outstanding performance towards electrooxidation reaction. However, the overall progress of fuel cells is severely restricted by the expensive and extremely scarcity of platinum. It is essential to provide effective strategies to decrease the demand of Pt and improve the atomic utilization, while maintaining the high catalytic performance [10,11]. As a significant challenge, various bimetallic Pt catalysts, such as Pt–Pb [12], Pt–Co [13,14], Pt–Cu [15], Pt–Rh [16] and Pt–Pd [17], have been studied, aiming at replacing the pure Pt catalysts. Pt-based bimetallic catalysts with transition elements can enhance the catalytic activity, owing to the lattice strain, downshift of the *d*-band center and possible synergistic effects [18]. Among bimetallic systems, Pt-Ni alloy has been emerged as the potential choice due to the promising characteristics towards the electrooxidation reactions [19–21].

During the research process for size controlling, morphology and facets of the nanostructure are also vital factors that determine crystal facets exposed and utilization efficiency of Pt atoms. In the broad variety of shapes, nanosphere [22], nanocube [23], octahedron [24], nanorod [25], nanowire [26], nanosheet [27], and so on, have been reported in the literature, tuning their properties and enhancing their application performances [28–30]. In particular, 2D nanowires or

* Corresponding author at: Laboratory of Alternative Energy Conversion Systems, Department of Mechanical Engineering, School of Engineering, University of Thessaly, Pedion Areos 38834, Greece.

** Corresponding author at: Collaborative Innovation Center of Sustainable Energy Materials, Guangxi Key Laboratory of Electrochemical Energy Materials, State Key Laboratory of Processing for Non-ferrous Metal and Featured Materials, Guangxi University, Nanning, 530004, PR China.

E-mail addresses: tsiak@mie.uth.gr (P. Tsiakaras), pkshen@gxu.edu.cn (P.K. Shen).

https://doi.org/10.1016/j.apcatb.2019.01.061
Received 1 December 2018; Received in revised form 12 January 2019; Accepted 19 January 2019
Available online 23 January 2019
0926-3373/ © 2019 Elsevier B.V. All rights reserved.

nanosheets can maximize the exposure of specific crystal faces, allowing them to exhibit further enhanced catalytic properties [31,32]. For example, Wang and co-workers have successfully synthesized high-purity Pt–Cu alloy ultrathin nanosheets, which show outstanding electrocatalytic activity for ethanol oxidation reaction in comparison to commercial Pt black and Pt/C catalysts [33]. Despite these achievements, they are only nanostructures in one-dimensional or two-dimensional plane, limiting the improvement in catalytic activity performance. Therefore, it is a strong demand to synthesize the nanosheets in three-dimensional plane.

Herein, we report a facile one-pot solvothermal method to synthesize the Pt–Ni cross double dumbbell-like nanostructures (CDDNs), which were composed of multiple nanosheets through a hub. The selective introduction of cetyl trimethyl ammonium chloride (CTAC) is a crucial step in the formation of CDDNs, which determines the direction of crystal growth. In addition to this, the presence of double dumbbell nanostructures with multiple 2D nanosheets provides open surface area and more active sites. More importantly, the Pt–Ni cross double dumbbell-like nanostructures exhibit an enhanced catalytic activity toward the oxygen reduction reaction and the methanol oxidation reaction in comparison with the ones obtained over commercial Pt/C and over self-made Pt–Ni electrocatalysts, as well as significantly increased the tolerance to CO poisoning.

2. Experimental

2.1. Materials

Platinum(II) acetylacetonate [$Pt(acac)_2$, 97%], nickel acetylacetonate [$Ni(acac)_2$, 95%], cetyl trimethyl ammonium chloride (CTAC, 97%), formaldehyde solution (37%), cetyl trimethyl ammonium bromide (CTAB), polyvinylpyrrolidone (PVP), trioctylphosphine oxide (TOPO), octadecyltrimethyl ammonium chloride (SATC) and oleylamine (OAM, 80-90%) were purchased from Aladdin. All chemical reagents were used as received without further purification. The water used here was ultrapure (18.2 MΩ).

2.2. Synthesis of Pt–Ni CDDNs and Pt–Ni nanoparticles

In a typical synthesis of *Pt–Ni CDDNs*, 10.1 mg $Pt(acac)_2$ were added into a solution containing 6.6 mg $Ni(acac)_2$, 100 mg CTAC, 0.6 mL formaldehyde solution and 10 mL OAM. The mixed solution was magnetically stirred for 30 min at room temperature. After that, the mixture was transferred to a 25 mL Teflon-lined stainless steel autoclave. The autoclave was then heated from room temperature to 160 °C, and kept for 12 h with magnetic stirring in an oil bath. The resulting colloidal product was collected and washed twice with hexane by centrifugation at 5000 rpm for 10 min.

In a typical synthesis of PtNi nanoparticles, 10.1 mg $Pt(acac)_2$ was added into a solution containing 6.6 mg $Ni(acac)_2$, 50 mg CTAB and 10 mL OAM. The other steps are the same as the synthesis of Pt-Ni CDDNs.

2.3. Preparation of carbon-supported catalysts

The Pt–Ni CDDNs and 10 mg commercial carbon (Vulcan-72) carbon were mixed in 20 mL *n*-butylamine solution. The solution was ultrasonicated for 2 h and then was stirred for three days. To remove excess organic matter and impurities, the product was placed in a furnace and annealed in air at 200 °C for 2 h. The Pt-Ni nanoparticles also adopt the same method.

2.4. Materials characterization

Transmission electron microscopy (TEM) images, high-angle annular dark-field scanning transmission electron microscope (HAADF-STEM) and energy-dispersive X-ray spectroscopy (EDS) observations were acquired on a FEI Titan ETEM $G^2$80-300, operating at an acceleration voltage of 300 kV. The samples for TEM characterizations were prepared by dropping ethanol dispersion of nanocrystals onto carbon-coated copper. To obtain crystal structure details, powder X-ray diffraction (XRD) characterization was performed by a Rigaku Corporation diffractometer with CuKa radiation. X-ray photoemission spectroscopy (XPS) tests were recorded with a Thermo Fisher Scientific ESCALAB 250 photoelectron spectrometer equipped with a monochromatic Al Kα X-ray source.

2.5. Electrochemical measurements

All electrochemical tests were recorded by a conventional three-electrode cell system with a computer-controlled bipotentiostat (PINE). A glassy-carbon (GC) rotating disk electrode (RDE) (area: 0.196 cm^2 - Pine Instruments) was used as working electrode, while a reversible hydrogen electrode (RHE) was used as reference electrode and a Pt flag as counter electrode. The catalyst ink was prepared by ultrasonically mixing 2.0 mg PtNi/C with 1.7 mL of ethanol, 300 μL of 0.05 wt% Nafion solution for 30 min. Afterwards, 10 μl of the as prepared ink suspension were deposited on the smooth glassy carbon electrode surface and dried naturally to form a uniform thin film at ambient condition. For the two types of Pt–Ni alloy electrocatalysts the Pt % on the Vulcan support was 30.0%. The Pt loadings were 15.29 μg cm^{-2} for Pt–Ni CDDNs, 15.30 μg cm^{-2} for Pt–Ni nanoparticles (NPs) and 21.44 μg cm^{-2} for commercial Pt/C, on the GC geometric electrode area of 0.196 cm^2. The electrochemical active surface areas (ECSAs) of the catalysts were estimated by hydrogen adsorption method. The ORR measurements were carried out in oxygen-saturated 0.1 M $HClO_4$ solutions. The ORR polarization curves were collected at 1600 rpm with scan rate of 10 mV s^{-1}. The potential was scanned from 0.05 to 1.1 V versus reversible hydrogen electrode (RHE). The accelerated durability test was performed in oxygen saturated 0.1 M $HClO_4$ solutions by potential cycling between 0.6 and 1.1 V versus RHE under a scan rate of 100 mV s^{-1} for 10,000 cycles.

For methanol oxidation, a three-electrode cell was also used. The saturated calomel electrode (SCE) was employed as reference electrode. Working and counter electrodes were the same as for ORR. The MOR measurements were carried out in 0.5 M H_2SO_4 aqueous solution containing 1 M CH_3OH. The stability tests were estimated by potential cycling treatment recorded for 1,000 cycles in a 0.5 M H_2SO_4 aqueous solution. All CV curves were obtained at a sweep rate of 50 mV s^{-1}, with scanning the potential from −0.2 to 1.0 V vs. SCE. For CO-stripping experiments, CO was used to saturate a 0.5 M H_2SO_4 aqueous solution for 30 min, holding the working electrode at −0.14 V vs. SCE. The remaining CO in the electrolyte was thoroughly purged with high purity N_2 gas for 15 min.

3. Results and discussion

3.1. Structure characterization of samples

The representative transmission electron microscopy (TEM) (Fig. 1a), high-angle annular dark-field scanning transmission electron microscopy (HAADF-STEM) (Fig. 1b) and scanning electron microscopy (SEM) images (Figure S1) show the microstructure of as-prepared products, displaying that the Pt–Ni nanostructures are composed of four nanosheets connected through an intermediate core (Fig. 1c). From these images, we can clearly distinguish that these nanoparticles are highly uniform in shape and the yield is extremely high (nearly 100%). These nanostructures show a particle size distribution with an average length around 42.3 ± 1.1 nm (Figure S2a). Transmission electron microscopy (TEM) images also confirm that the average diameter of nanosheets is about 37.5 ± 1.1 nm (Figure S2b) and the average thickness of nanosheets is around 5.5 ± 0.5 nm (Figure S2c), indicating the

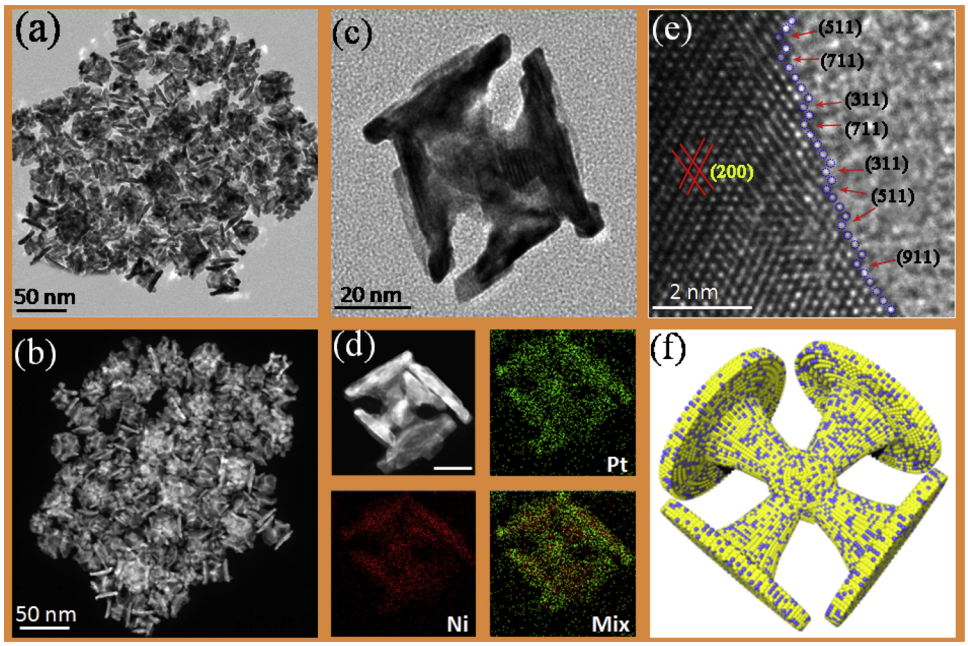

Fig. 1. (a) Low-magnification TEM image; (b) scanning transmission electron microscopy (STEM) image; (c) high-magnification TEM image of the Pt–Ni CDDNs; (d) HAADF-STEM image and elemental mapping images of a single cross double dumbbell-like Pt–Ni nanostructure; (e) atomic-resolution TEM image of the surface on the nanosheet; (f) the 3D schematic model of Pt–Ni CDDNs.

unique nanostructures possess relatively open surface area and high density atoms exposed on the surface.

According to the elemental mapping images of the individual nanoparticle obtained by HAADF-STEM-EDS (Fig. 1d), it is found that Pt and Ni elements are homogeneously distributed through the entire area, confirming an alloy structure.

More importantly, abundant stepped atoms and various high-index facets (HIFs), such as {511}, {311}, {911}, and {711}, are frequently observed around the nanosheets, which indicates that Pt-Ni CDDNs should exhibit much higher activity (Fig. 1e).

To identify the chemical compositions, the energy dispersive X-ray spectroscopy (EDS) analysis suggests that the atomic ratio of Pt/Ni is 61.1:38.9 (Fig. 2a), which is consistent with the inductively coupled plasma atomic emission spectroscopy (ICP-AES) results. In addition, Figure 1f illustrates the 3D schematic model of the Pt–Ni CDDNs.

To further characterize cross double dumbbell-like Pt–Ni nanostructures (CDDNs), a series of scientific instruments were used to analyze their unique morphology. Figure S3a shows the atomic-resolution HRTEM images marked from the red solid square 1, 2 and 3. As shown in Figure S3b, the observed lattice spacings (0.23 nm and 0.19 nm) in the core regions respectively correspond to the {111} and {200} planes of the Pt–Ni nanostructures. Moreover, the lattice spacing (0.19 nm) observed from the single nanosheet [Figure S3(c, d)] coincides with the (200) crystals planes of Pt–Ni alloy. Based on the investigations above and the corresponding fast Fourier transform (FFT) pattern (Figure S3), we can infer that the nanosheets grow along the < 100 > direction and indicate that the cross double dumbbell nanostructures have a fine crystalline nature.

The crystalline structure was further explored by X-ray diffraction (XRD). Fig. 2b shows the XRD patterns of the Pt–Ni CDDNs, the Pt–Ni nanoparticles (NPs) and the commercial Pt/C. The XRD spectra of the three kinds of nanostructures show several intense peaks, which can be clearly assigned to (111), (200), (220) and (311) diffractions of face-centered-cubic (fcc) crystal type. It is important to mention that each peak of two kinds of Pt–Ni nanostructures is slightly shifted to higher angles relative to Pt/C, indicating that Ni is incorporated into the Pt fcc structure to form an alloy phase with a concomitant lattice contraction, in agreement with the HRTEM results. No other special diffraction peaks are presented in the obtained patterns, suggesting that the crystallization of bimetallic Pt–Ni phase exists in a high quality.

X-ray photoelectron spectroscopy (XPS) is used to investigate the oxidation states and the surface compositions of the Pt–Ni CDDNs. Figure S4 illustrates the raw XPS intensity data of carbon-supported Pt–Ni CDDNs. As can be seen, the main peaks appear at 71, 285, 531 and 853 eV that well correspond to Pt, C, O and Ni elements, respectively. This proves that all the above elements are present in this investigation. The stronger Pt 4f peaks located at 71.55 and 74.95 eV from the high-resolution XPS spectrum [34] (Fig. 2c), which are well indexed to Pt 4f 7/2 and Pt 4f 5/2 of zero-valent state Pt; the weaker ones at 72.15 and 75.93 eV are attributed to the oxidation of the sample. The electronic structure and valence state of Ni was analyzed by a similar method (Fig. 2d). The percentage of Pt and Pt^{2+} is 1.51:1 and the percentage of Ni and Ni^{x+} is 1.42:1 in the surface of Pt-Ni CDDNs from the XPS test results. According to the results of XPS spectra, metallic Pt° and Ni° are predominant in the sample, owing to the higher peak intensity of Pt° and Ni° than that of Pt^{2+} and Ni^{x+}, showing an efficient reduction reaction of Pt and Ni precursor. On the basis of the XPS spectra, the atomic ratio of Pt/Ni is found to be 81.2/18.8, which is slightly higher than the above ICP-AES data. The difference in atomic ratio indicates a nanosheets' surface slightly reach with Pt, which is beneficial to improve the catalytic activity. Compared to the peak of Pt/C, the Pt 4f binding energy of Pt-Ni CDDNs is blue-shifted, which could be attributed to the Ni and Pt alloying, inducing the distinct change in the electronic structure of the alloy compared to the pure metal. In addition, the transformation of binding energy indicates the shifted *d*-band center relative to the Fermi level [35]. It reduces the adsorption of reaction intermediates on the surface of the nanostructures and thereby increases their catalytic activity.

In order to track the growth process of Pt–Ni CDDNs, time-dependent experiments were carried out to capture intermediate structures at different periods. After an initial growth period of 2 h, nanoparticles with polyhedral morphology and size of about 10 nm were obtained (Fig. 3a, Figure S5a). The EDS results show that the Pt/Ni atomic ratio is about 58.1/42.9 (Figure S5b), which is attributed to the standard redox potential for $PtCl_6^{2-}$/Pt (0.74 V vs RHE) that is more positive than Ni^{2+}/Ni (−0.25 V vs RHE). When extending the reaction time (the growth period) to 6 h, the cores of the nanoparticles begin to form multiple dendrites (Fig. 3b, Figure S5c). The atomic compositions of these nanocrystals are similar to the above EDS results (Figure S5d), and approaching to 3:2. Finally, at a reaction time of 12 h, the nanoparticles of branched nanostructures grew into cross double dumbbell-like morphology; that is, Pt–Ni CDDNs were obtained (Fig. 3c). Fig. 3e

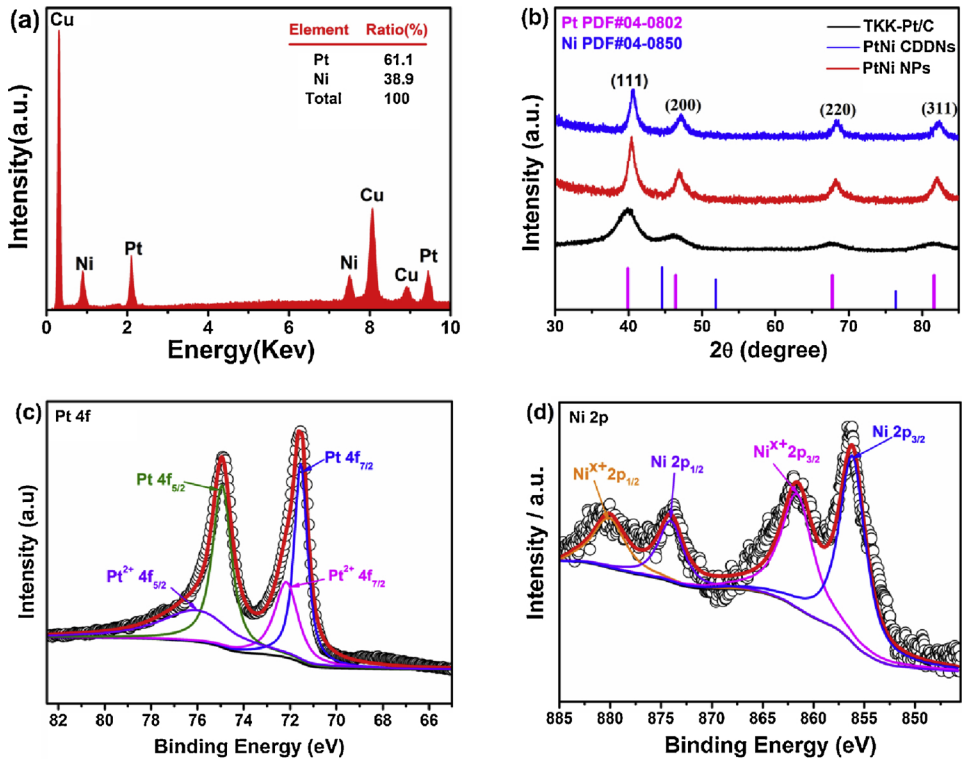

Fig. 2. (a) TEM-EDS spectrum of the Pt–Ni CDDNs, (b) X-ray diffraction patterns of Pt–Ni CDDNs, Pt-Ni NDs and commercial Pt/C, (c) Pt 4f XPS spectrum of Pt–Ni CDDNs and (d) Ni 2p XPS spectrum of Pt–Ni CDDNs.

shows the 3D schematic model of the Pt-Ni CDDNs for this evolution process. In addition, the influence of regent on the morphology was also investigated, while keeping all other experimental parameters constant in our synthesis. When no CTAC was introduced, we only observed some aggregated nanoparticles with an average size of 10 nm (Fig. 4a). When the amount of CTAC was increased to 50 mg we noticed a variety of morphologies, which also include some similar cross double dumbbell-like nanostructures (Fig. 4b). When the amount of CTAC was increased from 50 to 100 mg, in the standard procedure, we obtained the desired Pt–Ni CDDNs (Fig. 4c). In other words, the introduction of CTAC was found to be vital in controlling the formation of Pt–Ni CDDNs. Additionally, when CTAC is replaced by other surfactants, such as polyvinylpyrrolidone (PVP), trioctylphosphine oxide (TOPO) or octadecyltrimethyl ammonium chloride (SATC) (Figure S5), different phenomena were observed.

Under the conditions of replacement with these reagents, flower-like nanocrystals, irregular nanoparticles and nanodendrites were obtained [(Figure S6 (a, b, c)]. Combining these experimental results, it

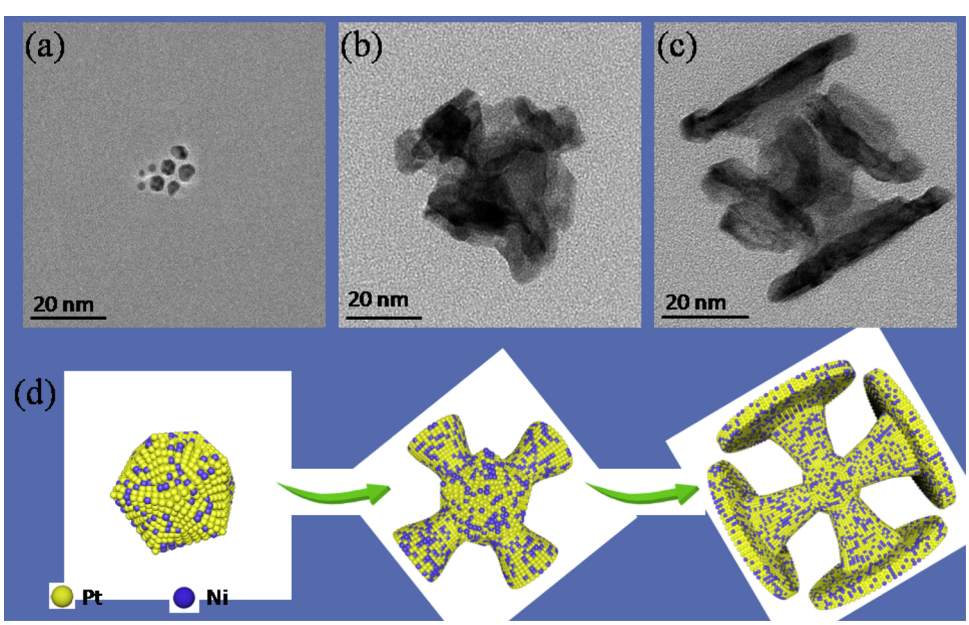

Fig. 3. STEM images of the products obtained at different reaction times: (a) 2, (b) 6 and (c) 12 h. (d) Schematic illustration of the corresponding products shown in (a)–(c) obtained at different reaction times.

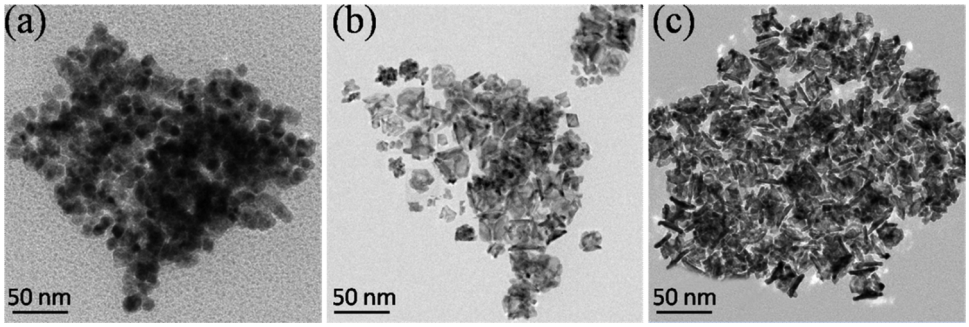

Fig. 4. (a) TEM images of Pt–Ni CDDNs prepared (a) without CTAC, (b) with 50 mg CTAC and (c) with 100 mg CTAC.

should be mentioned that an appropriate amount of CTAC is critical to form stable cross double dumbbell-like nanostructures and is identified to act as capping agent, indicating that each nanosheet grows along the < 100 > direction, as shown in HRTEM images (Figure S3).

On the basis of the above experimental explorations, we proposed a possible mechanism for the synthesis of Pt-Ni CDDNs. At the nucleation stage, the decomposition kinetics of Pt precursor is faster than that of Ni species, under the same conditions, because the standard redox potential for $PtCl_6^{2-}$/Pt (0.74 V vs RHE) is more positive than Ni^{2+}/Ni (−0.25 V vs RHE). Moreover, the single-crystalline polyhedron shows the thermodynamically relatively stable shape due to minimize the surface energy. Then, due to the selective capping of CTAC molecules on the facets, Pt and Ni atoms deposited on (100) facet, are promoting the polyhedral Pt-Ni nanostructures growing into branched structures along the < 100 > direction. As the reaction proceeds, due to the combined function of low concentration precursors and capping agents, the branched structures begin to grow laterally, and the lateral growth rate is much higher than the longitudinal growth rate, ultimately resulting in the formation of multiple nanosheets with larger size. Finally the cross double dumbbell-like Pt–Ni nanostructures are obtained.

3.2. ORR and MOR performance of the samples

As known, the Pt-based catalysts are the most active electrocatalysts for many electrocatalytic reactions, such as the oxygen reduction reaction and methanol oxidation reaction. In order to prove the actual application, the as prepared Pt–Ni CDDNs were tested for the ORR and MOR to show their natural advantage in electrocatalysis. The carbon-supported Pt–Ni CDDNs were prepared by loading Pt–Ni CDDNs on commercial carbon to make them uniformly dispersed. Before the electrochemical testing, Pt-Ni CDDNs were collected by centrifugation with ethanol and the working electrode was electrochemically cleaned by continuous potential cycling to remove the surfactant. In addition, commercial Pt/C (46.7% Pt, TKK, Japan) and self-made Pt-Ni nanoparticle catalysts (Figure S7) are considered as comparative objects under the same test conditions. First, the electrochemically active surface areas (ECSAs) of Pt–Ni CDDNs, of Pt-Ni nanoparticles and of commercial Pt/C catalyst were estimated though cyclic voltammetry (CV) measurements in N_2-saturated 0.1 M $HClO_4$ aqueous solution at a potential scan rate of 50 mV/s (Fig. 5a), adopting a value of 210 μC/cm^2 for the adsorption of hydrogen monolayer. The ECSAs are found to be 26.7 $m^2\ g_{Pt}^{-1}$ for Pt-Ni CDDNs and 29.5 $m^2 g_{Pt}^{-1}$ for Pt–Ni NCs, both smaller than that of the commercial Pt/C catalyst (43.3 $m^2 g_{Pt}^{-1}$). These ECSA results show that the as-prepared Pt–Ni CDDNs and Pt–Ni NCs indeed possess great advantages in maintaining high active surface area.

In the ORR test illustrated in Fig. 5b, are reported their representative polarization curves in O_2-saturated 0.1 M $HClO_4$ aqueous solution at a scan rate of 10 mV s^{-1} and rotation rate of 1600 rpm. The kinetic current was calculated using the Levich–Koutecky equation. Remarkably, the half-wave potential (0.93 V) of Pt–Ni CDDNs and the half-wave potential (0.89 V) of Pt–Ni NCs are both more positive than that of commercial Pt/C (0.87 V), highlighting the high ORR activity of Pt-Ni CDDNs alloy catalysts. For a better understanding of electrocatalytic activity, the mass activity of the three catalysts were also calculated (Fig. 5c).

Apparently, the Pt-Ni CDDNs catalysts possess the highest mass activity (1.33 A mg^{-1} Pt), which are 3.9 and 10.2 times higher that of the referenced Pt–Ni nanoparticles (0.34 A mg^{-1} Pt) and Pt/C catalysts (0.13 A mg^{-1} Pt), respectively. It suggests that the catalytic performance of Pt–Ni CDDNs is significantly improved due to their unique structures and specific compositions. Furthermore, the electrochemical durability of Pt–Ni CDDNs was evaluated by using accelerated durability tests (ADT), which were performed by cycling the potential between 0.6 and 1.1 V (*vs.* RHE) in O_2-saturated 0.1 M $HClO_4$ at a scan rate of 50 mV/s [Figure S8(a, b)]. After scanning for 10,000 cycles, the Pt–Ni CDDNs exhibit a relatively smaller negative shift. Moreover, as can be seen from Figure S8c, the Pt–Ni CDDNs still maintain a relatively high mass activity of 0.97 A mg^{-1} Pt, which is 7.5-fold enhanced compared with the one of commercial Pt/C. As a result, it is also show that Pt–Ni CDDNs exhibit a better durability compared to the commercial Pt/C catalyst.

Beyond ORR, the Pt–Ni CDDNs exhibited significantly enhanced activity and durability towards MOR, as compared to the Pt–Ni NCs and the commercial Pt/C catalysts. Fig. 6a shows the CV curves for the electrooxidation of methanol over the three kinds of catalysts, obtained in N_2-saturated 0.5 M H_2SO_4 aqueous solution at a scan rate of 50 mV s^{-1}. In the stable MOR CV curves (Fig. 6b), the Pt–Ni CDDNs show a mass activity of 3.02 A mg^{-1} Pt, which is 2.4 and 4.2 times higher than that of the Pt–Ni NCs (1.26 A mg^{-1} Pt) and the commercial Pt/C catalyst (0.72 A mg^{-1} Pt) (Fig. 6c). In addition, the Pt-Ni CDDNs display a much higher I_f/I_b ratio, in which I_f and I_b represent the forward and backward peak current density in MOR, respectively, compared to commercial Pt/C (1.21 vs. 0.35).

As demonstrated in previous reports, the aforementioned result indicates that the Pt–Ni CDDNs possess an enhanced anti-poisoning (poison tolerant) ability compared to the commercial Pt/C catalyst. To verify this assumption, we additionally performed CO stripping experiments. It is evident form Fig. 6d that Pt–Ni CDDNs are characterized by a high CO tolerance, higher than that of Pt–Ni NCs and of commercial Pt/C, as the peak potential of CO oxidation shifted negatively by 90 mV and 108 mV, respectively. In addition, as can be seen from Figure S9b, durability tests were carried out by sweeping the potential from −0.2 to 1.0 V (vs. SCE) in the N_2-saturated 0.5 M H_2SO_4 aqueous solution containing 1 M CH_3OH. After scanning for 1000 cycles, the peak current densities of Pt–Ni CDDNs and commercial Pt/C catalysts are about 82% and 58% of their initial values (Figure S9c), respectively. Moreover, the structures of the Pt–Ni CDDNs and Pt–Ni NPs were slightly changed during durability tests of ORR and MOR (Figure S10). XPS analysis shows that the Pt 4f spectra of Pt–Ni CDDNs and Pt–Ni NPs were very similar before and after electrocatalysis, while Ni 2p peaks slightly moved to a higher binding energy (Figure S11).

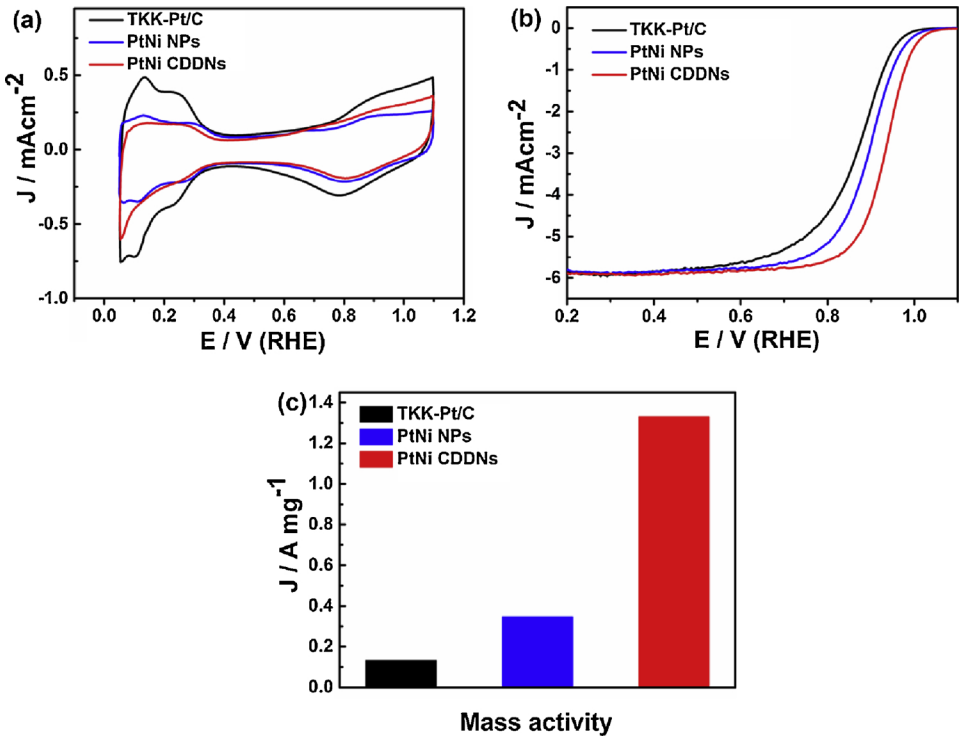

Fig. 5. (a) Cyclic voltammograms of Pt–Ni CDDNs, Pt–Ni NDs and TKK-Pt/C catalysts recorded at 50 mV s^{-1}, (b) ORR polarization curves of these catalysts recorded at 10 mV s^{-1} and (c) mass activity at 0.9 V versus RHE for these catalysts.

The enhanced electrocatalytic performance of Pt–Ni CDDNs toward ORR and MOR are attributed to the following reasons:

i) First, the Pt–Ni CDDNs with multiple 2D nanosheet structures provide a relatively large surface area with various HIFs (high-index facets), which possess many active sites. Meanwhile, the Pt-rich surface as revealed from the XPS results, can maximize utilization efficiency of Pt atoms.

ii) Second, previous studies have shown that the incorporation of a 3*d* transition metal into Pt can adjust the surface electronic properties of Pt, which could accelerate the reduction of O_2 molecules [36–38].

It has been proved that the lattice-mismatch strain in the Pt-Ni bimetallic alloy could lead to the downshift of the *d*-band center, which can weaken the adsorption energy between Pt and O and thus improve the electrocatalytic performance for ORR [39,40]. On the other hand, the presence of Ni would decrease the chemical adsorption of oxygen-containing species, such as CO, on the catalyst surface and thus enhance the CO tolerance during MOR. The synergistic effect between Pt and Ni is beneficial to enhance the reactions of oxygen reduction (ORR) and

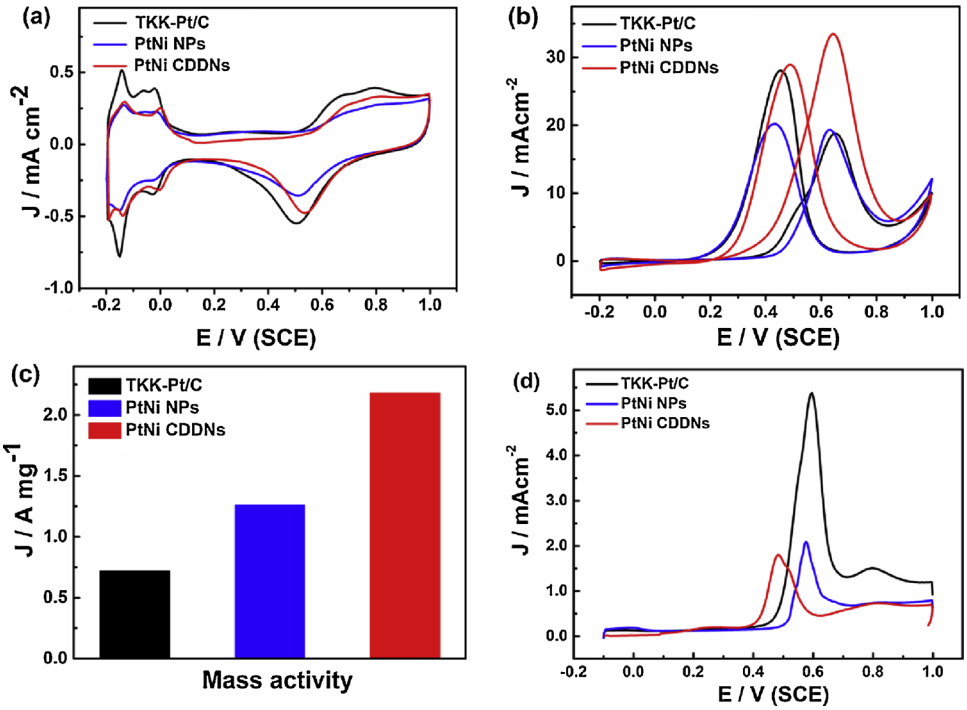

Fig. 6. Electrochemical measurements of the as-prepared Pt–Ni CDDNs, Pt–Ni NDs and commercial Pt/C catalysts. CV profiles recorded in (a) 0.5 M H_2SO_4 aqueous solution and (b) in 0.5 M H_2SO_4 + 1.0 M CH_3OH aqueous solution, (c) mass activity of the three catalysts at the peak potential and (d) CO-stripping voltammograms of Pt–Ni CDDNs, Pt-Ni NDs and commercial Pt/C in 0.1 M H_2SO_4 aqueous solution.

(MOR) methanol oxidation [41].

4. Conclusions

Concluding, in the present work Pt–Ni CDDNs (cross double dumbbell-like nanostructures) were facilely synthesized through a one-pot solvothermal strategy. A series of control experiments were designed to demonstrate that CTAC (cetyl trimethyl ammonium chloride) is considered essential for constructing this special structure morphology. More precisely, the selective use of CTAC promotes the nanosheets growing along the < 100 > direction, which is attributed to the selective capping and the manipulating of the reduction kinetics from it. In addition, the as-synthesized Pt–Ni CDDNs exhibit enhanced electrocatalytic activity toward both the ORR and MOR compared with the commercial Pt/C catalyst, as well as good CO tolerance, which are benefited from the synergistic effects between Pt and Ni atoms and the high specific surface area of nanosheets.

In this regard, we believe that the achievement of such unique structure will open up a new and efficient way toward the atomic-scale engineering of nano-frame structured materials for acquiring highly-performing catalysts for reactions occurred in various electrochemical devices for energy conversion and storage.

Acknowledgements

This work was supported by the Guangxi Science and Technology Project (AA17204083, AB16380030), National Basic Research Program of China (2015CB932304), the link project of the National Natural Science Foundation of China and Fujian Province (U1705252), the Natural Science Foundation of Guangdong Province (2015A030312007) and the Danish project of Initiative toward Non-precious Metal Polymer Fuel Cells (4106-000012B). Prof. Tsiakaras has been financially supported by the Ministry of Education and Science of the Russian Federation (Mega-Grant, contract no. 14.Z50.31.0001) and co-financed by the European Union and Greek national funds through the Operational Program Competitiveness, Entrepreneurship and Innovation, under the call RESEARCH – CREATE – INNOVATE (project code:T1EDK-02442).

Appendix A. Supplementary data

Supplementary material related to this article can be found, in the online version, at doi:https://doi.org/10.1016/j.apcatb.2019.01.061.

References

[1] H.L. Liu, F. Nosheen, X. Wang, Chem. Soc. Rev. 44 (2015) 3056–3078.
[2] C. Zhu, D. Du, A. Eychmuller, Y. Lin, Chem Rev. 115 (2015) 8896–8943.
[3] Q. Chen, Y. Jia, S. Xie, Z. Xie, Chem. Soc. Rev. 45 (2016) 3207–3220.
[4] K.D. Gilroy, A. Ruditskiy, H.C. Peng, D. Qin, Y. Xia, Chem Rev. 116 (2016) 10414–10472.
[5] A. Ruditskiy, H.C. Peng, Y. Xia, Annu. Rev. Chem. Biomol. Eng. 7 (2016) 327–348.
[6] M. Shao, Q. Chang, J.P. Dodelet, R. Chenitz, Chem. Rev. 116 (2016) 3594–3657.
[7] J. Wang, B. Li, T. Yersak, D. Yang, Q. Xiao, J. Zhang, C. Zhang, J. Mater. Chem. A 4 (2016) 11559–11581.
[8] X. Wang, A. Ruditskiy, Y. Xia, Natl. Sci. Rev. 3 (2016) 520–533.
[9] Y. Xia, Y. Xiong, B. Lim, S.E. Skrabalak, Angew. Chem. 48 (2009) 60–103.
[10] A.R. Tao, S. Habas, P. Yang, Small 4 (2008) 310–325.
[11] Y.C. Wu, Springer Theses 12 (2016) 2190–5053.
[12] X. Qu, Z. Cao, B. Zhang, X. Tian, F. Zhu, Z. Zhang, Y. Jiang, S. Sun, Chem. Commun. 52 (2016) 4493–4496.
[13] X. Huang, Y. Li, Y. Li, H. Zhou, X. Duan, Y. Huang, Nano Lett. 12 (2012) 4265–4270.
[14] L. Huang, Z. Jiang, W. Gong, P.K. Shen, ACS Appl. Nano Mater. 1 (2018) 5019–5026.
[15] S. Luo, M. Tang, P.K. Shen, S. Ye, Adv. Mater. 29 (2017) 1601687.
[16] H. Huang, K. Li, Z. Chen, L. Luo, Y. Gu, D. Zhang, C. Ma, R. Si, J. Yang, Z. Peng, J. Zeng, J. Am. Chem. Soc. 139 (2017) 8152–8159.
[17] A.X. Yin, X.Q. Min, Y.W. Zhang, C.H. Yan, J. Am. Chem. Soc. 133 (2011) 3816–3819.
[18] M. Shao, Q. Chang, J.P. Dodelet, R. Chenitz, Chem Rev. 116 (2016) 3594–3657.
[19] X. Huang, E. Zhu, Y. Chen, Y. Li, C.Y. Chiu, Y. Xu, Z. Lin, X. Duan, Y. Huang, Adv. Mater. 25 (2013) 2974–2979.
[20] A. Oh, H. Baik, S.C. Dong, J.Y. Cheon, B. Kim, H. Kim, S.J. Kwon, H.J. Sang, Y. Jung, K. Lee, ACS Nano. 9 (2015) 2856–2867.
[21] G. Niu, M. Zhou, X. Yang, J. Park, N. Lu, J. Wang, M.J. Kim, L. Wang, Y. Xia, Nano Lett. 16 (2016) 3850–3857.
[22] Y. Yu, W. Yang, X. Sun, W. Zhu, X.Z. Li, D.J. Sellmyer, S. Sun, Nano Lett. 14 (2014) 2778–2782.
[23] H. Du, S. Luo, K. Wang, M. Tang, R. Sriphathoorat, Y. Jin, P.K. Shen, Chem. Mater. 29 (2017) 9613–9617.
[24] M. Gocyla, S. Kuehl, M. Shviro, H. Heyen, S. Selve, R.E. Dunin-Borkowski, M. Heggen, P. Strasser, ACS Nano. 12 (2018) 5306–5311.
[25] H. Zhu, S. Zhang, S. Guo, D. Su, S. Sun, J. Am. Chem. Soc. 135 (2013) 7130–7133.
[26] K. Jiang, D. Zhao, S. Guo, X. Zhang, X. Zhu, J. Guo, G. Lu, X. Huang, Sci. Adv. 3 (2017) e1601705.
[27] L. Bu, N. Zhang, S. Guo, X. Zhang, J. Li, J. Yao, T. Wu, G. Lu, J.Y. Ma, D. Su, Science 354 (2016) 1410–1414.
[28] J. Gu, Y.W. Zhang, F.F. Tao, Chem. Soc. Rev. 41 (2012) 8050–8065.
[29] Z. Fang, Y. Wang, C. Liu, S. Chen, W. Sang, C. Wang, J. Zeng, Small 11 (2015) 2593–2605.
[30] Y. Kang, P. Yang, N.M. Markovic, V.R. Stamenkovic, Nano Today 11 (2016) 587–600.
[31] Y. Chen, Z. Fan, Z. Zhang, W. Niu, C. Li, N. Yang, B. Chen, H. Zhang, Chem Rev 118 (2018) 6409–6455.
[32] H. Jin, C. Guo, X. Liu, J. Liu, A. Vasileff, Y. Jiao, Y. Zheng, S.Z. Qiao, Chem Rev 118 (2018) 6337–6408.
[33] F. Saleem, Z. Zhang, B. Xu, X. Xu, P. He, X. Wang, J. Am. Chem. Soc. 135 (2013) 18304–18307.
[34] T. Xia, J. Liu, S. Wang, C. Wang, Y. Sun, L. Gu, R. Wang, ACS Appl. Mater. 8 (2016) 10841–10849.
[35] H. Fan, M. Cheng, Z. Wang, R. Wang, Nano Res. 10 (2016) 187–198.
[36] L. Han, H. Liu, P. Cui, Z. Peng, S. Zhang, J. Yang, Sci. Rep. 4 (2014) 6414–6416.
[37] V.R. Stamenkovic, B.S. Mun, K.J. Mayrhofer, P.N. Ross, N.M. Markovic, J. Am. Chem. Soc. 128 (2006) 8813–8819.
[38] V. Stamenkovic, B.S. Mun, K.J. Mayrhofer, P.N. Ross, N.M. Markovic, J. Rossmeisl, J. Greeley, J.K. Nørskov, Angew. Chem. 118 (2010) 2881.
[39] P. Strasser, S. Koh, T. Anniyev, J. Greeley, K. More, C. Yu, Z. Liu, S. Kaya, D. Nordlund, H. Ogasawara, Nat. Chem. 2 (2010) 454–460.
[40] J. Gu, Y.W. Zhang, F.F. Tao, Chem. Soc. Rev. 41 (2012) 8050–8065.
[41] Z. Zhang, Z. Luo, B. Chen, C. Wei, J. Zhao, J. Chen, X. Zhang, Z. Lai, Z. Fan, C. Tan, M. Zhao, Q. Lu, B. Li, Y. Zong, C. Yan, G. Wang, Z.J. Xu, H. Zhang, Adv. Mater. 28 (2016) 8712–8717.